Partial rupture of a locked patch of the Sumatra megathrust during the 2007 earthquake sequence

A. Ozgun Konca[1], Jean-Philippe Avouac[1], Anthony Sladen[1], Aron J. Meltzner[1], Kerry Sieh[1*], Peng Fang[2], Zhenhong Li[3], John Galetzka[1], Jeff Genrich[1], Mohamed Chlieh[4], Danny H. Natawidjaja[1], Yehuda Bock[2], Eric J. Fielding[5], Chen Ji[6], and Don V. Helmberger[1]

[1]Tectonics Observatory, Division of Geological and Planetary Sciences, California Institute of Technology, Pasadena, California 91125, USA. [2]Scripps Institution of Oceanography, University of California, San Diego, La Jolla, California 92093, USA. [3]COMET, Department of Geographical and Earth Sciences, University of Glasgow, Glasgow G12 8QQ, UK. [4]Geosciences Azur, Universite´ de Nice Sophia-Antipolis, Institut de Recherche pour le De´veloppement, Observatoire de la Cote d'Azurrue, 06560 Valbonne, France. [5]Jet Propulsion Laboratory, M.S. 300-233, California Institute of Technology, Pasadena, California 91109, USA. [6]Department of Geological Sciences, University of California, Santa Barbara, California 94106. *Present address: Earth Observatory of Singapore, Nanyang Technological University, 50 Nanyang Avenue, 639798 Singapore

The great Sumatra-Andaman earthquake and tsunami of 2004 was a dramatic reminder of the importance of understanding the seismic and tsunami hazards of subduction zones[1-4]. In March 2005, the Sunda megathrust ruptured again, producing an M_w 8.6 event[5] south of the 2004 rupture area, the site of a similar event in 1861[6]. Concern was focused on Mentawai area, where large earthquakes had occurred in 1797 (M_w 8.8) and 1833 (M_w 9.0) [6, 7]. A magnitude 8.4 and twelve hours later, a magnitude 7.9 earthquake indeed occurred on September 12, 2007. Here we show that these earthquakes ruptured only a fraction of the area ruptured in 1833, and consist of distinct asperities within a patch of the megathrust that had remained locked in the interseismic period. This indicates that the same portion of a megathrust can rupture in different patterns depending on whether asperities break as isolated seismic events or cooperate to produce a larger rupture. This variability probably arises from the influence of non-permanent barriers, zones with locally lower pre-stress due to the past earthquakes. The stress state on the portion of the Sunda megathrust that had ruptured in 1833 and 1797 was probably not adequate for the development of a single major large rupture in 2007. The moment released in 2007 amounts to only a fraction of that released in 1833, as well as of the deficit of moment that had accumulated as a result of interseismic strain since 1833. The potential for a large megathrust event in the Mentawai area remains large.

Slip along a subduction megathrust can be either aseismic or seismic. Seismic slip commonly has a duration of seconds to minutes, with sliding velocities of about a meter per second and rupture velocities of a few km/sec[8]. Such rapid failure generates strong ground shaking and tsunamis. Slower, aseismic slip is also common, and dominates at depths greater than about 40 km,[9] but also occurs at shallower depths [10-14]. This process leads to heterogeneous strain accumulation in the interseismic period with stress building up around locked patches that presumably end up failing during megathrust earthquakes.

The modeling of geodetic and paleogeodetic measurements of interseismic strain indeed shows that the Sunda megathrust offshore Sumatra consists of a patchwork of creeping and locked areas[15] (Fig. 1) and suggests some correlation between megathrust earthquakes and interseismic coupling. A recent example of this is the rupture of a 350-km section, in the 2005, M_w 8.6, Nias earthquake[5]. Historical accounts[6]

and paleoseismic data[16] indicate that rupture of about the same patch produced an earlier great earthquake in 1861. Immediately south of the Nias patch, near the equator, coupling is low and consistent with only moderate earthquakes in the past few centuries [10, 17]. Farther south, beneath the Mentawai Islands, coupling has been high for at least the past 40 years and great earthquakes have occurred repeatedly [18]. These observations indicate that the pattern of interseismic strain accumulation has a profound influence on the characteristics of large megathrust ruptures.

Figure 1 | Patches with strong interseismic coupling on the Sunda megathrust, offshore Sumatra, coincide with large seismic ruptures. The pattern of coupling, defined as the ratio of interseismic slip rate to plate convergence rate, is derived from the modeling of geodetic and paleogeodetic data[15]. No information is available on coupling under northern Simeulue, west of about 96.2°E. Slip distribution of the 2005 M_w 8.6 earthquake of 2005 is shown with 5 meter contour lines in green[1112]. Gray and black polygons show estimated rupture areas of the 1797 and 1833 earthquakes [25]. Dark and pale blue lines show the 1 m and 5 m slip contour lines of the M_w 8.4 and 7.9 seismic ruptures of 2007, stars show the epicenters. The smaller M_w 7.7 earthquake of 1935 [17] occurred in a region of weak coupling. The M_w 8.0 earthquake of 2000 which is predominantly an intraslab strike-slip event [30] also falls in an area with low coupling, The inset map displays various asperities of the 2007 rupture sequence.
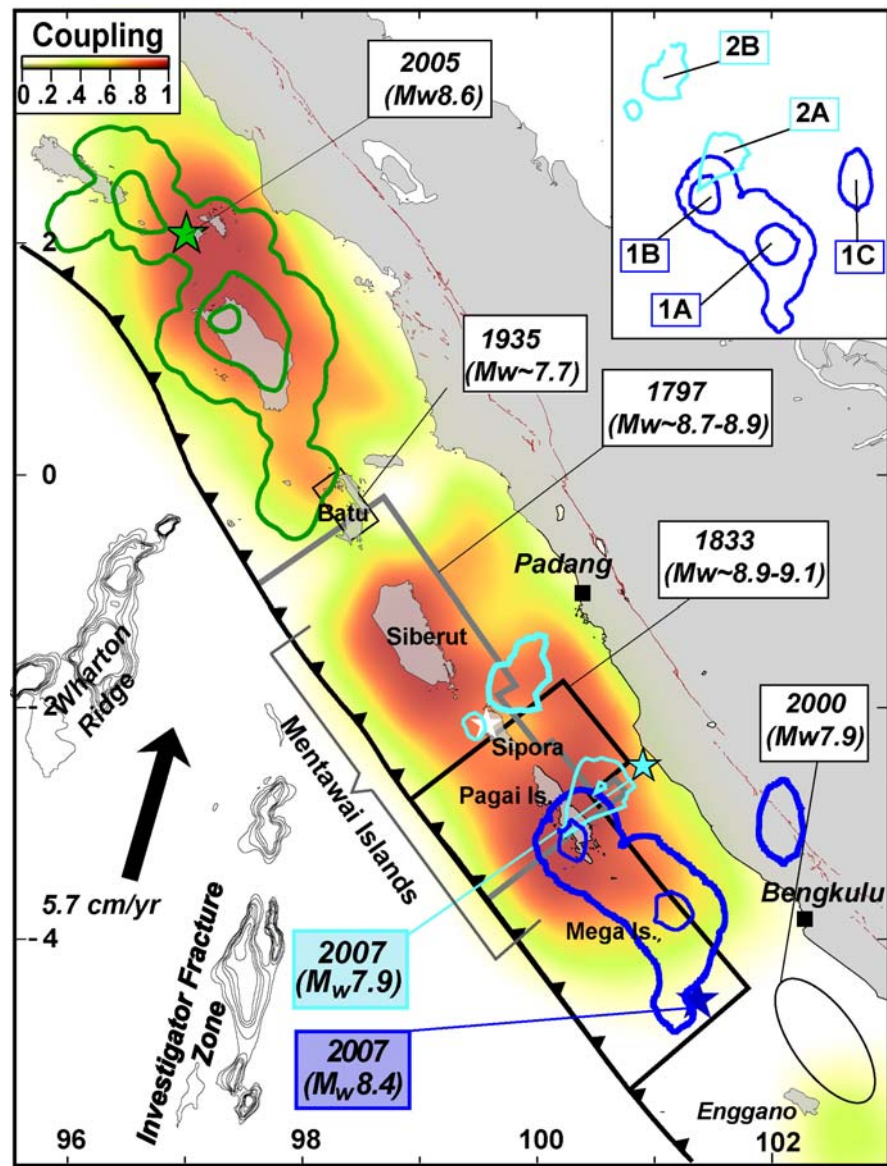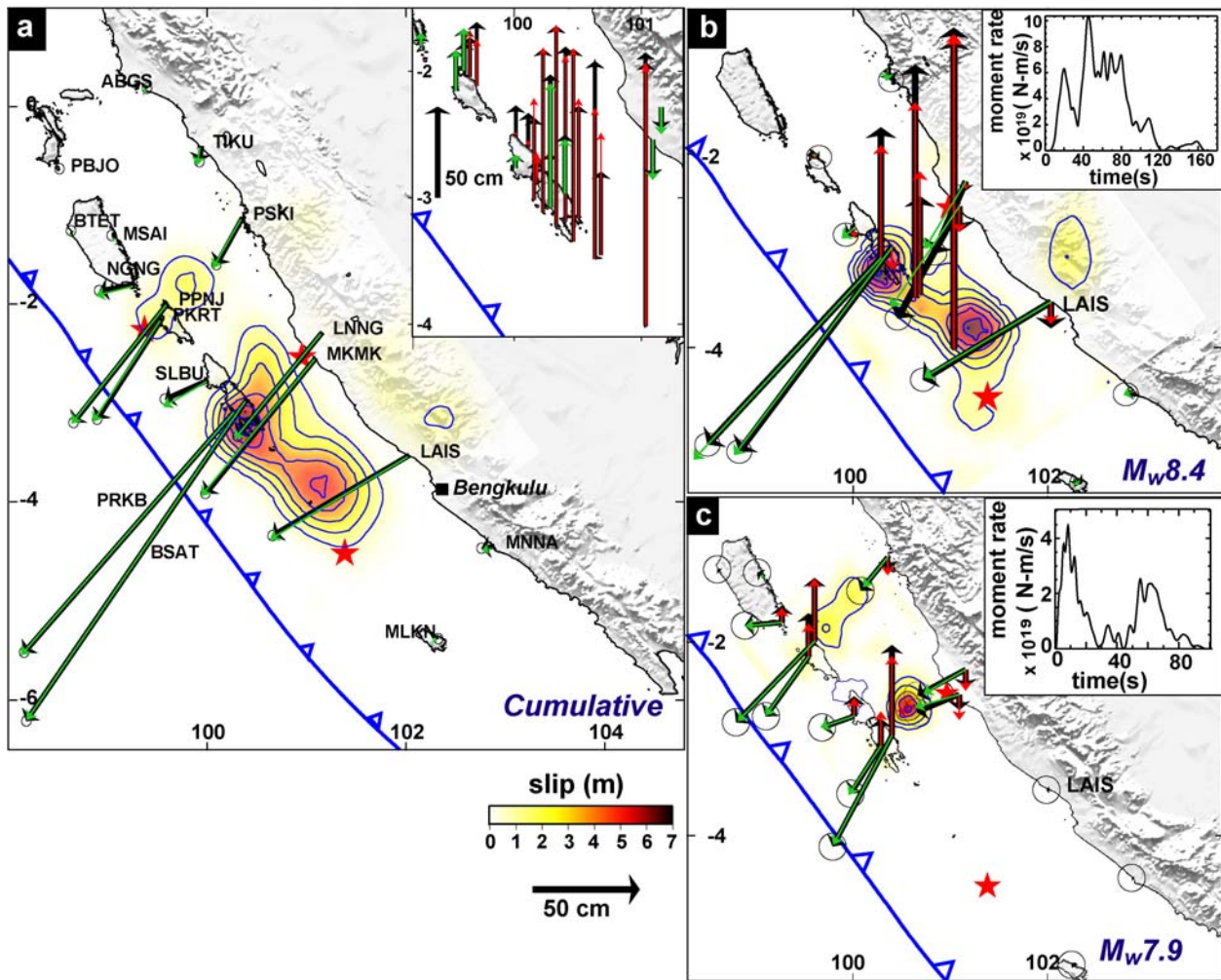
Figure 2 | Models of megathrust slip during the M_w 8.4 and M_w 7.9 earthquakes show principal slip on widely separated patches. All slip models and GPS vectors are plotted with scales displayed on bottom left. Slip contour lines are plotted every 1 m starting at 1 m. **a.** Cumulative slip distribution due to the M_w 8.4 and 7.9 earthquakes of September, 12, 2007. Contours show cumulative slip of best-fitting inversion of the GPS, coral and InSAR data. Vectors are observed (black) and modeled (green) horizontal displacement values at the SuGAr cGPS stations. Normalized error ellipses are also shown. Inset shows the vertical GPS displacements and measurements of coral uplift (black) and the fits from the model (green for GPS, red for coral). **b,** Slip model of the M_w 8.4 earthquake obtained from the joint inversion of teleseismic waveforms, GPS data, InSAR data, and measurements of coral uplift unambiguously attributable to the M_w 8.4 event. Observed displacements, shown with error ellipses in black, originate at the GPS station locations and coral sites. Modeled horizontal and vertical vectors are green and red, respectively. Red stars represent the USGS locations of epicenter. Inset shows moment rate function. Geodetic data are tabulated and fits to the InSAR and teleseismic data are shown in the Supplements. **c,** Model of the M_w 7.9 earthquake from the joint inversion of teleseismic waveforms and GPS measurements. Vector color coding is the same as in Fig. 2b. Inset shows that the moment was released in two discrete episodes, about 20 s apart. Fits to the teleseismic data are shown in the Supplements.

Nonetheless, successive seismic ruptures in the same area may differ significantly in extent and magnitude[19-21]. This paper provides an exceptionally well-documented case of such variability. We show that the 2007 sequence of large seismic ruptures on the strongly coupled Mentawai patch differs significantly from previous ruptures of this section in 1833 and 1797. The slip and extent of the recent ruptures are far smaller than during these previous historical events. Moreover, the recent events released far less moment than the deficit of moment that has accumulated since the previous great earthquakes.

We use GPS measurements, field measurements of uplift, SAR interferometry, and seismological records to estimate the source parameters of the two large earthquakes of September 12, 2007. Details are given in Supplements. The 2007 ruptures occurred beneath a large subset of the continuously recording GPS (cGPS) stations of the Sumatran GPS Array (SuGAr) (http://www.tectonics.caltech.edu).
Displacements assigned to each of the events were determined from the 120-second time series. By contrast, the InSAR and field measurements provide information only on the cumulative effects of the sequence of earthquakes. These measurements cover greater lengths of time and therefore must include some amounts of postseismic deformation as well. All horizontal GPS motions are trenchwards (Fig. 2a). The maximum horizontal displacement due to the cumulative effect of the whole sequence, 1.5 m, occurred at station BSAT on South Pagai Island. Vertical displacements were measured at the GPS stations and from the emergence or submergence of coral microatolls on the reefs that fringe the Mentawai Islands. They show uplift of the islands and subsidence of the mainland coast (inset in Fig. 2a). The maximum uplift reaches 1.3 m on Mega Island, about 70 km northwest of the epicenter. Uplift decreases northwards to about 1 m on southern South Pagai

to 10 cm on North Pagai Island. Uplift at Sipora Island is on the order of 20 cm. These data are complemented with InSAR line-of-sight displacements. We processed four independent interferograms from ALOS PALSAR images using ROI_PAC software[22]. These data are consistent with the GPS and coral measurements where they coincide and provide a much denser spatial coverage. They show a strong gradient of displacement under Pagai Islands and reveal a zone of deformation beneath north of Bengkulu on Sumatra mainland (Supplementary Fig. S1).

We determine static and kinematic source models from the modeling of the surface displacements and teleseismic waveforms recorded at a selection of IRIS stations chosen to assure a good azimuthal coverage. The geometry of the megathrust is approximated by a plane dipping 15° to the north-east, away from the trench. We also computed models assuming a curved fault geometry with the dip angle increasing with depth (see Supplement for details). These tests show that the results described here are independent of the assumed geometry of the megathrust. We first determined a cumulative slip model that includes both the M_w 8.4 and M_w 7.9 earthquakes using the cGPS cumulative displacements, the field measurements of uplift, and the InSAR data. The model obtained using only the cGPS displacements measured from just before the M_w 8.4 to just after the M_w 7.9 is the least contaminated by postseismic relaxation. It suggests a relatively patchy slip distribution with a geodetic moment of 7.3×10^{21} N.m (Supplementary Fig. S2a). The spatial resolution of the model improves when the InSAR and field data are added, but some contamination by postseismic deformation is introduced. In fact, the best-fitting model calculated from all these data (Fig. 2a) has a total moment of 7.5×10^{21} N.m (equivalent to $M_w = 8.5$), which is only marginally larger than the one derived from the cGPS measurements alone. Thus we regard this

source model to be a better-constrained representation of the coseismic slip distribution than the model derived from only GPS data. This cumulative source model is also very similar to the model obtained by adding up the M_w 8.4, 7.9

The cumulative slip model (Fig. 2a) has a dumbbell-shaped principal rupture area extending contiguously northwestwards from the hypocenter, offshore Bengkulu, to South Pagai. There are in addition two disconnected minor slip patches. One is below northern Sipora Island, about 100 km along strike of the northwest edge of the principal rupture. The other lies beneath the volcanic arc of the mainland, about 100 km down-dip from the down-dip edge of the principal rupture. Slip peaks at 8 m on the main patch under southern South Pagai Island and at 5 m local maxima about 25 km northeast of Mega Island. The maximum slip on the small patch beneath Sipora Island is 2.5 m. All datasets are fitted well with slip on a single plane representing the megathrust; slip on any other fault is therefore not required.

We also derived separate kinematic source models of the mainshock and principal aftershock utilizing teleseismic waveforms, GPS measurements, and subsets of the coral and InSAR data. For this analysis, we discarded data from the Pagai Islands, where the contributions from each of the two events cannot be distinguished. Farther south and east, the displacements measured along PALSAR track 445 and coral measurements on Mega Island, are clearly attributable to the mainshock alone (see details in Supplements, Section H). We modeled these subsets of the coral and InSAR data together with the GPS measurements and the teleseismic records of the mainshock.

The source model of the M_w 8.4 mainshock shows unilateral northward rupture, which initiated about 70 km south of Mega Island (Fig. 2b). As in the cumulative source model, the most prominent slip loci are under southern

and a 7.0 aftershock models (Supplementary Figure S2b). The greater resolution afforded by the coral and InSAR measurements implies that the patchiness of the slip distribution is real and not an artifact of our methodology.

South Pagai Island, where slip peaks at about 7 m, about 25 km north of Mega Island, where slip peaks at about 6 m, and on the deep patch east of the Sumatran coast (Fig. 1 inset). The total seismic moment of this model ($\sim 5 \times 10^{21}$ N.m) is consistent with the GCMT moment magnitude (http://www.globalcmt.org/). Source-time function indicates that the rupture was not very impulsive and lasted for about 100 s (Fig. 2b inset). The rise times are estimated to be 5–10 s, and the moment rate increased smoothly over the first 20 s (Supplementary Fig. 5). The southern patch slipped during the first 40 s and the northern patch slipped between 40 s and 80 s.

The model of the 7.9 aftershock derived from the joint inversion of the teleseismic and cGPS data shows that this earthquake also involved failure of more than one discrete patch (Fig. 2c). The 1.1×10^{21} N.m moment of this event was released in two pulses over about 80 s. (Fig 2c inset). Rupture initiated within a few km of the down-dip edge of the mainshock's northern patch. The seismic waveforms require an extremely abrupt initiation of the first subevent (rise times of a few seconds at most) and a highly peaked slip distribution around the hypocenter. The second subevent occurred in 50–80 s and about 130 km farther northwest of the epicenter, east of northeastern Sipora Island. There is no evidence for significant slip between these two subevents.

The September 2007 sequence ruptured a number of distinct asperities (defined here as patches with locally large slip) on the megathrust that lie within a patch that had remained strongly locked in the interseismic period and also lie within the rupture area of the 1833 earthquake (Fig. 1). However, the patterns and amounts of slip in 1833 and 2007 are significantly different. Coseismic uplifts in 1833 (between 1 and 2.5 m

from South Pagai to Sipora Island)[7], are much larger than those observed in 2007. This is consistent with the cumulative 7.5×10^{21} N.m geodetic moment released by the 2007 earthquake sequence, representing a fraction of the $10\text{–}55 \times 10^{21}$ N.m released in 1833[15] (Fig. 3). The coast of North Pagai Island was uplifted by

2.2 m in 1833[18]. This area is clearly a low-slip patch in 2007, as indicated by the modest horizontal and vertical displacements recorded at SLBU (22cm and 7cm, respectively). Thus, it acted more like a 'barrier' during the coseismic slip in 2007.

Figure 3 | The earthquakes of 2007 are far smaller than would be needed to relieve all moment deficit accumulated between 2007 and the previous great earthquakes in 1797 and 1833. Light gray curves are the upper and lower bounds of estimated moment release for the 1833 and 1797 earthquakes, based on modeling of geodetic and paleogeodetic data[15] and taking into account effect of 20 % postseismic slip. The confidence intervals were deduced from the uncertainty on the extent of the ruptures and on the eventual contribution of postseismic deformation to the vertical displacements deduced from by the coral data. Purple curve shows accumulated moment deficit since the last great rupture, derived from the modeling of interseismic strain accumulation (Fig. 1, model J-a of Chlieh[15]). Moment-deficit values are integrals within bins that are a half degree of latitude wide.
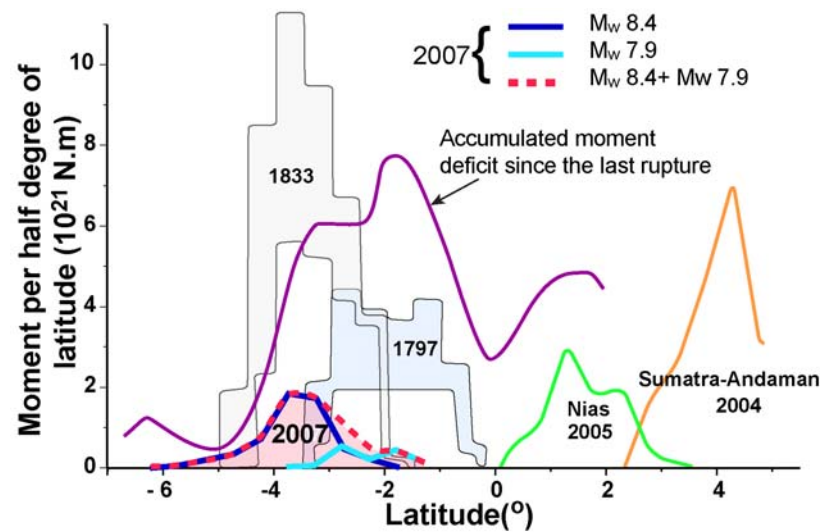
South of 2° S, the moment deficit accumulated since 1833 is still less than the moment released during the 1797 and 1833 events (Fig 3). North of 2° S, the accumulated deficit is far greater than the moment released during the 1797 and 1833 events. Thus, one might have expected the next great rupture to occur north of 2° S. Instead, the 2007 events occurred south of 2° S. Furthermore, the moment released during the 2007 sequence is far less than that released during the 1833 event and far less than what has accumulated since then. These relationships demonstrate clearly that the Mentawai patch is behaving in neither a slip- nor a time-predictable manner. If rupture were time-predictable, slip would already have occurred

north of 2° S. If rupture were slip-predictable, slip would have been far greater in 2007 south of 2° S.

A striking question is why the 2007 sequence did not duplicate the 1833 event and why it released only about 25% of the deficit of moment that had accumulated since 1833. The 2007 sequence consisted of several spatially and temporally separate asperities which probably did not cooperate effectively. If two neighboring asperities on the same fault plane rupture jointly, they are expected to cooperate to release more moment than if they had ruptured independently[24]. This is because the static stress change induced by one asperity increases the

stress on the other, hence the elastic stress that is released during the rupture. Spatiotemporal evolutions of the 2007 ruptures show that this kind of cooperation was not effective. For example, slip on the second asperity of the M_w 7.9 earthquake (2B in Fig. 1) started only once the slip on the first asperity (2A) was over. So the reloading of asperity 2A due to rupture of asperity 2B did not contribute to any additional slip. This might be because the intervening area between the two asperities acted as a barrier to the rupture propagation. This intervening area beneath North Pagai Island experienced little coseismic slip in 2007, but is probably not a permanent barrier since the same area experienced the largest cumulative slip (of about 17 m), if the slip models from 1797 and 1833 earthquakes are summed[7]. This area may therefore have acted as a barrier in 2007 because of a locally lower stress level before the earthquake, left over from previous earthquakes. Minimal cooperation between the rupture of asperities 1B and 2A is also evident from the 12-hour time lag between their ruptures. The cause of the lack of cooperation between these two asperities is more enigmatic, given that they lie so close. A narrow zone with low pre-stress due to the slip distribution related to the 1833 and 1797 events may have acted as a barrier, or there might be a creeping zone too narrow to show up in the pattern of interseismic strain. In any case, it appears that the static stress increase on asperity 2A due to the M_w 8.4 earthquake was enough to trigger a delayed rupture of this asperity. By contrast, the dynamic stresses induced by the M_w 8.4 earthquake failed to trigger the rupture of asperity 2A.

Two independent SAR interferograms and the GPS displacement at LAIS show that the M_w 8.4 rupture induced a localized surface deformation just north of Bengkulu, and that this deformation took place during the earthquake, even though it did not contribute much to the seismic radiation (see details in Supplement). It is possible to model this signal as a deep slip patch on the megathrust that falls in a zone that creeps in the interseismic period (asperity 1C in Fig. 1). Because this slip patch is isolated, we exclude the possibility that it would be due to the rupture propagating into the rate-strengthening zones. It could reflect seismic rupture of a rate-weakening portion of the megathrust embedded in a dominantly creeping zone, or it may be an example of a triggered aseismic transient. Deep aseismic transients on megathrusts have been observed[14] and justified based on rate-and-state friction theory[25, 26]. Another possibility is that this deformation did not take place on the megathrust but at shallower depths. The available data do not resolve this ambiguity.

In conclusion, the rupture area of the 2007 Mentawai earthquakes was confined to a subset of a locked portion that is surrounded by creep during the interseismic period. Such permanent barriers, which are found to influence the down-dip as well as the lateral extent of megathrust ruptures, can be imaged from the modeling of interseismic strain[2, 12-14], except when they lie in stress shadows along the up-dip portion of the plate interface [11]. The complex spatiotemporal pattern of the 2007 rupture is probably related to the fact that it produced much less slip than historical earthquakes in the area. The 2007 ruptures released only 25% of the deficit of moment that had accumulated since the last rupture. The sequence essentially ruptured a set of asperities, which triggered each other through static and dynamic interactions, but did not cooperate efficiently because of the intervening barriers. Some of these barriers are most likely not permanent and are related to the slip in past earthquakes. While permanently creeping barriers should tend to favor some regularity and similarity of earthquakes, non-permanent barriers due to the stress distribution left over from previous ruptures is probably the major factor that is introducing irregularity, as observed in dynamic fault models[27, 28]. This is likely the main reason that neither the slip-predictable nor the time-predictable models apply, and why the 2007 earthquakes didn't

grow as big as in 1833. This adds to the view that seismic asperities are probably not permanent features[29] but rather move around from one rupture to another within the area that is locked in the interseismic period.

Method

It is assumed that the seismic rupture can be modeled as the propagation of a rupture front with finite width. The kinematic source model is then characterized by the static slip, the rupture velocity and the rise-time, the time it takes for slip at a point on the fault to reach its final static displacement, at each elementary patch. The joint inversion consists of searching for the model that best fits the wavelet transform of the seismograms, the geodetic and InSAR data. We use an optimization method based on simulated annealing algorithm, where bounded parameter spaces of slip amplitude, rake angle and rupture velocity are searched to obtain models that fit both teleseismic and geodetic data[23]. In practice, rupture velocity is allowed to vary between 2.1 and 2.8 km/s, and the rake angle can vary between 80˚ and 130˚. We selected teleseismic waveforms from the IRIS network to assure a good azimuthal coverage in order to constrain the source model. The broadband seismograms were bandpass filtered from 1.5 s (P-waves) and 3 s (SH-waves) to 200 s. We have used 16 P and 19 SH waveforms for the M_w 8.4 earthquake, and 19 P and 17 SH waveforms for the M_w 7.9 earthquake. The duration of the waveforms used for modeling the earthquake was 120 seconds for both the M_w 8.4 and M_w 7.9 earthquakes. Details on the GPS and InSAR data and inversion method are given in Supplement.

References

1. Lay, T. et al. The great Sumatra-Andaman earthquake of 26 December 2004. Science 308, 1127-1133 (2005).
2. Chlieh, M. et al. Coseismic slip and afterslip of the great M-w 9.15 Sumatra-Andaman earthquake of 2004. Bulletin of the Seismological Society of America 97, S152-S173 (2007).
3. Ammon, C. J. et al. Rupture process of the 2004 Sumatra-Andaman earthquake. Science 308, 1133-1139 (2005).
4. Subarya, C. et al. Plate-boundary deformation associated with the great Sumatra-Andaman earthquake. Nature 440, 46-51 (2006).
5. Briggs, R. W. et al. Deformation and slip along the Sunda Megathrust in the great 2005 Nias-Simeulue earthquake. Science 311, 1897-1901 (2006).
6. Newcomb, K. & McCann, W. Seismic History and Seismotectonics of the Sunda Arc. J. Geophys. Res. 92, 421-439 (1987).
7. Natawidjaja, D. H. et al. Source parameters of the great Sumatran megathrust earthquakes of 1797 and 1833 inferred from coral microatolls. Journal of Geophysical Research-Solid Earth 111 (2006).
8. Ruff, L. & Kanamori, H. Seismic Coupling and Uncoupling at Subduction Zones. Tectonophysics 99, 99-117 (1983).
9. Pacheco, J. F., Sykes, L. R. & Scholz, C. H. Nature of Seismic Coupling Along Simple Plate Boundaries of the Subduction Type. Journal of Geophysical Research 98, 14133-14160 (1993).
10. Sieh, K., Ward, S. N., Natawidjaja, D. & Suwargadi, B. W. Crustal deformation at the Sumatran subduction zone revealed by coral rings. Geophysical Research Letters 26, 3141-3144 (1999).

11.   Burgmann, R. et al. Interseismic coupling and asperity distribution along the Kamchatka subduction zone. Journal of Geophysical Research-Solid Earth 110 (2005).

12.   Suwa, Y., Miura, S., Hasegawa, A., Sato, T. & Tachibana, K. Interplate coupling beneath NE Japan inferred from three-dimensional displacement field. Journal of Geophysical Research-Solid Earth 111 (2006).

13.   Freymueller, J. T. & Beavan, J. Absence of strain accumulation in the western Shumagin segment of the Alaska subduction zone. Geophysical Research Letters 26, 3233-3236 (1999).

14.   Pritchard, M. E. & Simons, M. An aseismic slip pulse in northern Chile and along-strike variations in seismogenic behavior. Journal of Geophysical Research-Solid Earth 111 (2006).

15.   Chlieh, M., Avouac, J.-P., Sieh, K., Natawidjaja, D. H. & Galetzka, J. Heterogeneous coupling on the Sumatra megathrust constrained from geodetic and paleogeodetic measurements. J. Geophys. Res., (in press).

16.   Meltzner, A. J. et al. in Eos, Transactions, American Geophysical Union (2007).

17.   Natawidjaja, D. et al. Paleogeodetic records of seismic and aseismic subduction from central Sumatran microatolls, Indonesia. Journal of Geophysical Research 109, doi:10.1029/2003JB0002398 (2004).

18.   Natawidjaja, D. H. et al. Interseismic deformation above the Sunda Megathrust recorded in coral microatolls of the Mentawai islands, West Sumatra J. Geophys. Res. 112 (2007).

19.   Thatcher, W. Order and diversity in the modes of Circum-Pacific earthquake recurrence. J. Geophys. Res. 95, 2609-2623 (1990).

20.   Ando, M. Source mechanisms and tectonic significance of historical earthquakes along Nankai Trough, Japan. Tectonophysics 27, 119-140 (1975).

21.   Lay, T., Kanamori, H. & Ruff, L. The Asperity Model and the Nature of Large Subduction Zone Earthquakes. Earthquake Prediction Research 1, 3-71 (1982).

22.   Rosen, P. A., Henley, S., Peltzer, G. & M., S. Updated Repeat Orbit Interferometry Package Released,. Eos Trans. AGU 85, 47 (2004).

23.   Ji, C., Wald, D. & Helmberger, D. V. Source Description of the 1999 Hector Mine, California Earthquake, Part I: Wavelet Domain Inversion Theory and Resolution Analysis. Bull. Seismol. Soc. Am. 92, 1192-1207 (2002).

24.   Rundle, J. B. & Kanamori, H. Application of an Inhomogeneous Stress (Patch) Model to Complex Subduction Zone Earthquakes - a Discrete Interaction Matrix Approach. Journal of Geophysical Research-Solid Earth and Planets 92, 2606-2616 (1987).

25.   Perfettini, H. & Ampuero, J. P. Dynamics of a velocity strengthening fault region: Implications for slow earthquakes and postseismic slip. Journal of Geophysical Research (2008).

26.   Liu, Y. & Rice, J. R. Aseismic slip transients emerge spontaneously in three-dimensional rate and state modeling of subduction earthquake sequences. J. Geophys. Res. 110, B08307 (2005).

27.   Ben-Zion, Y. & Rice, J. R. Earthquake Failure Sequences Along a Cellular Fault Zone in a 3-Dimensional Elastic Solid Containing Asperity and Nonasperity Regions. Journal of Geophysical Research-Solid Earth 98, 14109-14131 (1993).

28.   Cochard, A. & Madariaga, R. Complexity of seismicity due to highly rate-dependent friction. Journal of Geophysical Research-Solid Earth 101, 25321-25336 (1996).

29.   Park, S. C. & Mori, J. Are asperity patterns persistent? Implication from large earthquakes in Papua New Guinea. Journal of Geophysical Research-Solid Earth 112 (2007).

30.   Abercrombie, R. E., Antolik, M. & Ekstrom, G. The June 2000 M-w 7.9 earthquakes south of Sumatra: Deformation in the India-Australia Plate. Journal of Geophysical Research-Solid Earth 108, art. no.-2018 (2003).

Partial rupture of a locked patch of the Sumatra megathrust during the 2007 earthquake sequence

A. Ozgun Konca[1], Jean-Philippe Avouac[1], Anthony Sladen[1], Aron J. Meltzner[1], Kerry Sieh[1], Peng Fang[2], Zhenhong Li[3], John Galetzka[1], Jeff Genrich[1], Mohamed Chlieh[4], Danny H. Natawidjaja[1], Yehuda Bock[2], Eric J. Fielding[5], Chen Ji[6], and Don V. Helmberger[1]

Supplementary Information

A. GPS data and processing

The data processing was carried out using GAMIT/GLOBK version 10.31 (http://chandler.mit.edu/~simon/gtgk/GAMIT_Ref_10.3.pdf). A total of 9 days of observations from 2007 Sept 8 to Sept 16 were used. Data, sampled at a 120 s interval, were processed in daily sessions except on the days of the M_w 8.4 and 7.9 earthquakes. On these days we computed sub-daily sessions from the set of 120s samples determined before and after each quake. For each session, a regional network is formed consisting of the regional sites and selected nearby global sites. The global sites are: COCO, DGAR, GUAM, IISC, NTUS, PERT and TIDB. International GNSS Service (IGS) final orbits (http://igscb.jpl.nasa.gov) and International Earth Rotation Service (IERS Bulletin-A) final earth orientation parameters (http://maia.usno.navy.mil) were used with tight constraints. Standard corrections were applied including solid earth tides, pole tide, and ocean tides. Tropospheric delay parameters were estimated at one hour intervals.

After completing individual daily/sub-daily sessions using GAMIT, the loosely constrained solutions were sorted into four groups: one before the 1st quake, one after the 1st quake and before the 2nd, one after the 2nd and before the 3rd, and one after the 3rd. They were input to the GLOBK software and combined with SOPAC final global solutions (http://garner.ucsd.edu/pub/solutions/global) in order to tie the solutions to the ITRF2005 global reference frame http://itrf.ensg.ign.fr/ITRF_solutions/2005/ITRF2005.php. The formal uncertainties for individual sites for those 4 grouped time segments are given in Tables S1-S3. The data can be visualized and downloaded from the Caltech Tectonics Observatory web site (http://www.tectonics.caltech.edu/sumatra/data.html).

Co-seismic offsets are measured as the difference of the average position determined from the position time series between the two earthquakes, compared to linear least squares adjustment of the position time series before the 1st and after the 2nd earthquake. This process allows measuring the sudden offset at the time of each earthquake.

B. Measurements of uplift from emerged coral heads

Coral microatolls of the genus *Porites* are sensitive natural recorders of lowest tide levels [1-4], and as such they are ideal natural instruments for measuring emergence or submergence relative to a tidal datum. Massive *Porites* coral heads grow radially upward and outward until they reach an elevation that exposes their highest corallites to the atmosphere during lowest tides. This subaerial exposure kills the uppermost corallites in the colony, thus restricting future upward growth. The highest level to which a coral can grow is termed the highest level of survival (HLS). If a coral microatoll is then uplifted or

subsides, its morphology preserves information about relative water level prior to the land level change [2, 4].

When coseismic uplift occurs, those portions of the microatoll colony raised above lowest tides die, but if lower parts of the coral head are still below lowest tides, its uppermost living tissues demarcate a new, post-earthquake HLS [2]. Coral microatolls have been shown to track annual low tide (ALT, the lowest low tide of any given year) with an accuracy of a few centimeters, [3] and the difference between pre-earthquake and post-earthquake HLS can be taken as the amount of uplift. In cases of subsidence or where post-earthquake HLS cannot be found, the elevation change can be determined using the pre-earthquake HLS and post-earthquake calculated ALT[4, 5].

The corals revealed significant uplift of Mega Island, South Pagai Island, and the northern tip of Sipora Island. The maximum uplift measured from corals was 1.3 m, on Mega Island, about 70 km northwest of the epicenter. Uplift decreases northward to about 1 meter on southern South Pagai, to 10 cm on North Pagai Island. The uplift on northern Sipora Island is on the order of 20-30 cm (inset in Figure 2a, Table S4).

C. InSAR data and processing

We processed four independent L-band interferograms from ALOS PALSAR images using the ROI_PAC software[6] and the satellite orbits provided by JAXA with the PALSAR data (Table S5). The topographic phase contribution was removed using a 3 arc.s (~90 m) digital elevation model from the Shuttle Radar Topography Mission (SRTM)[7]. The interferograms were next unwrapped to obtain line-of-sight (LOS) displacements, i.e., along a direction that is pointing approximately N78^{o}E with an incidence angle of 38° from vertical. Typical PALSAR raw data in the Fine Beam Single (FBS) polarization mode has a row width of ~10500 pixels, exactly twice that of Fine Beam Double (FBD) polarization images [8]. In order to make a mixed-mode interferogram (FBS2FBD) for track 445, the FBD was up-sampled by FFT [9].

Even in heavily vegetated areas, coherence is generally good and deformation is well resolved, highlighting the main advantage of L-band (wavelength of 23.53 cm) over C-band (wavelength of 5.66 cm): i.e. less temporal decorrelation due to its capability to penetrate more deeply in vegetation. The track 448 pair, in which coherence degrades rapidly in areas of rugged terrain in the south part of South Pagai Island, is explained by the large perpendicular baseline (506 m, Table 1). Because most interferograms do not extend far enough from the area with significant ground displacements, possible orbit knowledge errors were not corrected a priori. Instead, we allow for a ramp correction (first order polynomial) in the LOS displacement field that is solved for during the joint inversion.

The interferograms were unwrapped using the SNAPHU algorithm [10]. The unwrapped interferograms were resampled by averaging phase with variable block sizes using a fault slip resolution-based algorithm [11] and are shown in Figure 2b. The resampling process reduced the number of InSAR data samples from millions to about 400 samples per interferogram. The LOS vector was approximated as constant over the PALSAR tracks.

InSAR data show that there is strong gradient in displacement under the Pagai Islands (track 448), while displacement under Siberut is insignificant (track 450). The tracks along the Sumatra coast show a deep

slip patch near Bengkulu (track 445 and 446). Overall, the InSAR data is in very good agreement with cGPS and coral data.

D. Effect of post-seismic slip on the geodetic data and Cumulative Model

We have used three different sets of geodetic data—continuous GPS (cGPS), InSAR and coral uplift measurements—to model the cumulative slip from the 2007 Sumatra sequence (Figure 2a). Inspection of the time series shows that the co-seismic displacements measured from cGPS data are probably not biased by post-seismic deformation. By contrast, the coral and InSAR measurements cover a time span which is longer than the coseismic earthquake duration, over which some postseismic deformation occurred as the GPS time series reveal. Post-seismic horizontal displacements in the month following the earthquakes are as great as 15% of the coseismic signal, but for the stations with the largest offsets (BSAT, PRKB) they remain less than 10 % of the co-seismic offset measured from the daily solution. Preliminary modeling show that postseismic deformation is due mainly to rapidly decaying afterslip updip of the rupture area (as was observed following the M_w 8.6 Nias-Simeulue earthquake[12]) and released a geodetic moment of about 10^{21}N.m over the 125 days following the mainshock, representing about 15% of the co-seismic moment.

Pre-earthquake images of the InSAR data were acquired in the month prior to the earthquake except one track (track 445) where the pre-earthquake image was obtained 9 months before the earthquakes. Acquisition of the post-earthquake images occurred between 4 days and 43 days after the earthquake. The GPS time series shows that the preseismic signal in these data is insignificant. The postseismic signal, however, could represent as much as 15% of the signal measured on Siberut (track 450) and Pagai Islands but is probably a smaller fraction of the signal measured from the other tracks, since they were all acquired less than 20 days after the mainshock (Table S5). The coral measurements were made 2.5 to 4 weeks after the earthquake (Table S4). Therefore these measurements might also be influenced by post-seismic motion of up to 15 % of the measurement values.

One way to test effect of the post-seismic slip in our cumulative model from all geodetic data (cGPS, InSAR and corals) is to compare it to the models that do not include coral and InSAR data. Figure S2a shows a cumulative slip model obtained using only the cGPS displacements measured from just before the M_w 8.4 to just after the M_w 7.9. The model using cGPS data only, suggests a relatively patchy slip distribution with a geodetic moment of 7.3×10^{21}N.m. The best-fitting model calculated from all three geodetic datasets (Figure 2a) has a total moment of 7.5×10^{21} N.m (equivalent to M_w 8.5) which is only marginally larger than the one derived from the cGPS measurements alone.

The cumulative source model from all geodetic data is also very similar to the cumulative slip obtained by adding up the coseismic slip models of M_w 8.4 and M_w 7.9 earthquakes along with an M_w 7 aftershock located at the northwest tip of Sipora (Figure S2b; see Table S6 for model parameters). The model obtained by the addition of individual events is more confined along dip and has a lower moment (6.3×10^{21}N.m). This implies that including coral and InSAR data does introduce some post-seismic contamination. Nevertheless, the models obtained from cGPS only and from the addition of coseismic slips are very similar to the geodetic model utilizing all available data. Considering the advantage of greater resolution afforded by the coral and InSAR measurements, we regard the source model using all geodetic data to be a better-constrained representation of the cumulative slip distribution.

E. *Fault geometry*

There are no good geophysical constraints on the megathrust geometry in the Mentawai area. The global Centroid-Moment Tensor solutions show a dip angle of about 9° for the M_w 8.4 and 19° for the M_w 7.9 event (http://www.globalcmt.org/) that might suggest lateral variations, down-dip variations, or variations in both, of the dip angle.

However, for simplicity we have approximated the megathrust geometry as a planar fault dipping 15° to the northeast. This dip angle is consistent with the geometry of the megathrust beneath the forearc as can be inferred from various geophysical data including relocated seismicity[13], seismic profiles[14] and gravity modeling. [15] We found that we can reconcile all the data to first order from this simple assumption.

The modeled mainshock fault plane consists of 16 km by 16 km sub-faults, whereas the fault plane is more finely gridded (12 km by 10 km) for the M_w 7.9 event. In order to test the sensitivity of our results to the assumed megathrust geometry we also computed a model assuming an increase of the dip angle from 10º beneath the Mentawai Islands to 20º beneath the forearc basin and Sumatra mainland coastal area (Figure S3). Figure S3 shows for example the slip distribution obtained from the modeling of coral, cGPS and InSAR data. The slip distribution is only slightly different from that obtained with the reference single planar fault model. The total released moment, 7.79×10^{21} N.m, is only 9% higher. The number and the location of the main asperities, as well the values of the peak slip are nearly identical to the reference model as well.

F. Resolution Test

We have carried out checkerboard tests to evaluate the spatial resolution in our inversions (Figure S4). This approach only applies to the geodetic models which are in fact the key data constraining the geographic distribution of the slip. The resolution of the joint inversions must be similar or even better due to the additional constraints brought by the seismic waveform modeling, but this cannot be tested easily from checkerboard tests.

We constructed two checkerboard models, one with 48×48 km patches and the other with 80×80 km patches. We computed the corresponding theoretical displacements at the cGPS stations and at the location where coral data were collected, and the synthetic InSAR data a well (Figure 2a). The results of the checkerboard tests show that the slip patches of 80 km by 80 km are well resolved over most of the study area (Figure S4a). The 48 km by 48 km slip patches (Figure S4b) are well resolved in the Pagai and Sipora islands area and beneath the mainland, where most of the slip actually occurred in the 2007 events. The slip patches to the south of the Pagai Islands are not well resolved at this scale.

G. Source models of the M_w 8.4 and M_w 7.9 earthquakes

We derived separate source models of the mainshock (M_w 8.4) and principal aftershock (M_w 7.9) using teleseismic waveforms, GPS measurements, and subsets of the coral and InSAR data. To guide selection of the coral and InSAR data relevant to the modeling of each event we first carried out an inversion of just the teleseismic data first and then included the GPS data. The slip distribution derived from the inversion of the teleseismic waveforms only are shown in Figure S5 (details on these models are available at http://www.tectonics.caltech.edu/slip_history/index.html). The fit to the teleseismic and

InSAR data, of the source models derived from joint inversion for the M_w 8.4 and 7.9 earthquakes, respectively, are shown in Figures S6 and S7.

The source model of the M_w 8.4 earthquake derived from the inversion of the teleseismic waveforms show a rather diffuse slip distribution with slip spread along the isochrons. This is typical for teleseismic models when the source is not very impulsive, as is the case here, and is usually more severe for subduction earthquakes which tend to be wider along dip than crustal earthquakes. Although these models fit the teleseismic records very well they are not consistent with the geodetic data. When the GPS data are included in the inversion, the fit to seismological data is not degraded; this shows that the two dataset are consistent but that the GPS data put tighter constraints on the spatial distribution of slip. The geodetic data show that slip was confined to a narrower zone along dip with a larger maximum slip than the teleseismic inversion suggests (Figure S8). The teleseismic model of the M_w 7.9 earthquake (Figure S5b) is closer to the model derived from the joint inversion (Figure 2c). This is because the sharp initial pulse in the teleseismic waves (Figure S7) requires rupture of a rather compact first asperity near the hypocenter. The teleseismic records also require a second asperity which is estimated to lie near Sipora Island from the inversion.

Separating the effects of the two events on the measured co-seismic displacements in the region of the Pagai Islands, where their rupture areas abut or overlap, is most challenging. In this region, the coral and InSAR measurements (PALSAR track 448 from the Pagai Islands and track 446 from the Sumatra mainland coast, Figure S1) contain components from both events. Farther south and east, the displacements measured along PALSAR track 445 and coral measurements on Mega Island are clearly attributable to the mainshock alone. Since track 445 includes only 4 days of post-seismic slip, we chose to take it into account to constrain the source of the mainshock. We inverted these subsets of the coral and InSAR data together with the GPS measurements and the teleseismic records of that earthquake. We initially used the US Geological Survey (USGS) hypocenter and origin time (http://earthquake.usgs.gov/) to model the earthquakes. The M_w 8.4 earthquake model fits the teleseismic waveforms and geodetic data very well using the hypocenter reported by the USGS (lon: 101.382°, lat:-4.517°).

Fitting the geodetic and teleseismic data of the M_w 7.9 earthquake was more challenging when epicenter reported by USGS was used. The cGPS measurements on the Sumatra mainland show subsidence and modest horizontal displacements, while the measurements on South Pagai Island reveal significant uplift and more trenchward horizontal displacement (Figure 2c). Therefore, cGPS data require a slip patch just east of South Pagai Island (Figure 2c). In addition, sharp initial pulses in teleseismic waveforms require a slip patch centered at the hypocenter. We were unable to fit the geodetic and teleseismic data using the epicenter reported by USGS (lon: 100.964°, lat: -2.525°), which is just offshore the Sumatra mainland. Obtaining satisfactory fits to both datasets requires that the hypocenter lies at the center of the slip patch that is constrained from geodesy. Thus, we moved the M_w 7.9 epicenter east of South Pagai (lon: 100.5°, lat: -2.75°), about 55 km southwest of the USGS epicenter, and were thus able to reconcile all the data reasonably well. So, the addition of the geodetic and InSAR data essentially lead to some slight shift of the geographic location of the two asperities derived from the inversion of the teleseismic records alone.

H. Significance of the surface deformation north of Bengkulu

Both the GPS and InSAR data indicate a deep slip patch beneath an area north of Bengkulu. The evidence from cGPS data comes from LAIS station, which subsided only 10 cm but moved 70 cm

trenchwards during the M_w 8.4 mainshock. Assuming that all the slip has occurred on the megathrust, the only plausible explanation of this low ratio of vertical to horizontal displacement is to invoke some slip patch east of this station (Figure S9). Varying the dip angle does not improve the fits to the GPS data from LAIS station unless slip on downdip side of this station is allowed. The fault geometry with a depth dependent dip angle reveals the same result (Figure S3). The two InSAR tracks along the Sumatra coast (tracks 445 and 446 of Figure S1) provide a much denser spatial coverage and help constrain the shape and location of this slip patch (Figure 2b, Figure S3). Since the deformation is observed in these two independent tracks, the possibility of an atmospheric artifact can be excluded.

This deep slip patch had to occur during the mainshock rupture, because the sampling rate at LAIS is 120 s and the displacements shown in Figure 2b occurred within the 120-s period that includes the mainshock. The corresponding moment of this patch is around 6.3×10^{20} N.m (~M_w 7.8) assuming a shear modulus of 67.5 GPa. Despite the significant moment release, whether this patch radiated some seismic energy is unclear. Removal of the patch from the mainshock model yields only marginally different seismic waveforms and source time function (Figure S10).

In our model, the megathrust dips uniformly 15 degrees from the trench, so that this slip patch lies at a depth of about 90 km. It is more plausible, however, that the megathrust lies at a depth of about 120 km at the location of the patch given that the dip angle must increase down-dip. Another possibility would be that this deformation did not take place on the megathrust but at shallower depths. The available data do not resolve the ambiguity.

I. *Goodness of fit criterion and normalization of uncertainties*

In order to obtain the best-fitting models, we use an optimization method based on simulated annealing algorithm, where bounded parameter spaces of slip amplitude, rake angle and the rupture velocity are searched to obtain models that fit both teleseismic and geodetic data[16].

The seismic modeling requires fitting the wavelet transform of seismograms. The seismic displacements are calculated by

$$u(t) = \sum_{j=1}^{n} \sum_{k=1}^{m} D_{jk} \cdot Y_{jk}\left(\vec{x}, t - d_{jk}/V_{jk}\right) \dot{S}_{jk}(t) , \quad (1)$$

where $u(t)$ is the displacement at the station, j and k are indices of summation along strike and dip, respectively, Y_{jk} are the sub-fault Green's functions, D_{jk} the dislocations, V_{jk} are the rupture velocities between the hypocenter and sub-faults and d_{jk} are the distance of the sub-fault from the hypocenter. The rise time for each element is given by $S_{jk}(t)$. Both the V_{jk}'s and $S_{jk}(t)$'s control the timing of the contribution from each sub-fault. We approximate the latter as a modified cosine function defined by one parameter, as first proposed by Cotton and Campillo[17]. These seismograms are then transformed to wavelet domain to use the time and frequency variations in the signal simultaneously.

The misfit between the observation and synthetic waveforms is then quantified by the sum of L1 and L2 norms of the seismograms in different wavelet channels:

$$e_l = \sum_{j=j_{min}}^{j=jc} w_j \cdot \left(\frac{1}{k_j} \sum_{k}^{k_j} \left| o_{j,k} - y_{j,k} \right| + \sqrt{\frac{1}{k_j} \sum \left(o_{j,k} - y_{j,k} \right)^2} \right), \quad (2)$$

where $o_{j,k}$ and $y_{j,k}$ are the wavelet coefficients of the observed and synthetic seismogram for station k and wavelet index j, w_j are the weight of each wavelet channel [18].

The Green's functions used to compute the static ground displacement are calculated using the method developed by Xie and Yao[19]. We compare the observed and predicted displacements based on the mean weighted sum of the squares of the residuals (equivalent to a reduced chi-square criterion, except that this quantity doesn't account for the number of parameters entering the model) defined as:

$$\chi_r^2 = \frac{1}{n} \sum_{i=1}^{i=n} \left(\frac{(pred^i - ob^i)}{\sigma_i} \right)^2, \quad (3)$$

where n is the number of geodetic data, σ_i is the uncertainty associated for the each measurement ob^i, $pred^i$ is the predicted displacement at site i. Because uncertainties on the InSAR data cannot be reliably estimated a priori, and because the uncertainties assigned to the GPS and coral data may not have comparable statistical meaning, we estimated a posteriori normalized uncertainties such that each data set has a reduced chi-square of 1. The normalized uncertainties assigned to each type of data were computed from the standard deviation of the misfits between the considered subset of data and the predictions of the best-fitting model derived from the joint inversion. This is achieved through an iterative scheme so that the reduced chi-square (3) calculated from the best fitting final model equals approximately 1 when only one single type of data is taken into account. The normalized uncertainties are listed in Table S6.

We have also calculated the χ_r^2 (which can also be called the mean of Weighted Residual Sum of Squares mWRSS) between the observed GPS and coral measurement and the predictions of the various models (Table S7). It shows that the residuals between the predicted and observed GPS displacements are much larger than the formal uncertainties assigned to the GPS measurements. If uncertainties were not normalized, the inversion results would be constrained almost only by the GPS data.

In addition to geodetic and seismic misfit, we constrain the solution by requiring minimization of slip difference between adjacent faults [smoothing] and minimizing the moment difference from an *a priori* value [moment constraint]. The objective function is

$$misfit = e_{WF} + W_{ST} e_{ST} + Wsm \cdot e_{SM} + W_{MO} \cdot e_{MO} \ , (4)$$

where e_{WF} is the waveform error, W_{ST} is the weight of the static data, e_{ST} is static data error, w_{SM} and e_{SM} are weight and error for smoothness, respectively and w_{MO} and e_{SM} are weight and error for moment constraint, respectively.

All inversions start with a random initial model. The weight of the static error is then chosen to be equal to the waveform error. Weights of the constraining parameters are determined by trial and error. As the bound parameter space is searched, the objective function is minimized with 800 iterations.

References

1. Scoffin, T. P. & McLean, R. F. Exposed limestones of the northern province of the Great Barrier Reef. Philosophical Tranactions Royal Society of London, Series A 291, 119-138 (1978).
2. Taylor, F. W., Frohlich, C., Lecolle, J. & Strecker, M. Analysis of Partially Emerged Corals and Reef Terraces in the Central Vanuatu Arc - Comparison of Contemporary Coseismic and Nonseismic with Quaternary Vertical Movements. Journal of Geophysical Research-Solid Earth and Planets 92, 4905-4933 (1987).
3. Zachariasen, J., Sieh, K., Taylor, F. & Hantoro, W. S. Modern vertical deformation at the Sumatran subduction zone: Paleogeodetic Insights from Coral Microatolls. Bull.Seism.Soc.Am. 90, 897-913 (2000).
4. Briggs, R. W. et al. Deformation and slip along the Sunda Megathrust in the great 2005 Nias-Simeulue earthquake. Science 311, 1897-1901 (2006).
5. Meltzner, A. J. et al. Uplift and Subsidence Associated with the Great Aceh-Andaman Earthquake of 2004. Journal Of Geophysical Research 111, doi: 10.1029/2005JB003891 (2006).
6. Rosen, P. A., Henley, S., Peltzer, G. & M., S. Updated Repeat Orbit Interferometry Package Released,. Eos Trans. AGU 85, 47 (2004).
7. Farr, T. G. et al. The Shuttle Radar Topography Mission. Rev. Geophys. 45, RG2004 (2007).
8. Shimada, M., Isoguchi, O., Tadono, T., Higuchi, R. & Isono, K. in IGARSS07 (Barcelona, 2007).
9. Sandwell, D., Mellors, R., Shimada, M., Brooks, B. & Foster, J. Accuracy and Resolution of ALOS Interferometry: Vector Deformation Maps of the Father's Day Intrusion at Kilauea, . IEEE Geoscience and Remote Sensing Letters (2007).
10. Chen, C. W. & Zebker, H. A. Phase unwrapping for large SAR interferograms: statistical segmentation and generalized network models: . IEEE Transactions on Geoscience and Remote Sensing 40, 1709-1719 (2002).
11. Lohman, R. B. & Simons, M. Some thoughts on the use of InSAR data to constrain models of surface deformation: Noise structure and data downsampling. Geochem. Geophys. Geosyst 6 (2005).
12. Hsu, Y. J. et al. Frictional afterslip following the 2005 Nias-Simeulue earthquake, Sumatra. Science 312, 1921-1926 (2006).
13. Engdhal, E., van der Hilst, R. & Buland, R. Global teleseismic earthquake relocation with improved travel times and procedures for depth determination. Bulletin of the Seismological Society of America 88, 722-743 (1998).
14. Kieckhefer, R. M., Sho, G. G. & Curray, J. R. Seismic refraction studies of the Sunda trench and forearc basin. Journal of Geophysical Research 85, 863-889 (1980).
15. Simoes, M., Avouac, J. P., Cattin, R. & Henry, P. The Sumatra subduction zone: A case for a locked fault zone extending into the mantle. Journal of Geophysical Research-Solid Earth 109 (2004).
16. Ji, C., Wald, D. & Helmberger, D. V. Source Description of the 1999 Hector Mine, California Earthquake, Part I: Wavelet Domain Inversion Theory and Resolution Analysis. Bull. Seismol. Soc. Am. 92, 1192-1207 (2002).

17.   Cotton, F. & Campillo, M. Stability of the Rake During the 1992, Landers Earthquake - an Indication for a Small Stress Release. Geophysical Research Letters 22, 1921-1924 (1995).

18.   Ji, C., Wald, D. J. & Helmberger, D. V. Source description of the 1999 Hector Mine, California, earthquake, part I: Wavelet domain inversion theory and resolution analysis. Bull. Seism. Soc. Amer. 92, 1192-1207 (2002).

19.   Xie, X. & Yao, Z. X. A generalized reflection-transmission coefficient matrix method to calculate static desplacement field of a dislocation source in a stratified half space. Chinese Journal of Geophysics 32, 191-205 (1989).

20.   Shimada, M., Isoguchi, O., Tadono, T., Higuchi, R. & Isono, K. in IGARSS07 (Barcelona, Spain, 2007).

Figure S1 | Cumulative model fits to the InSAR data. InSAR data, and fits from the cumulative model of Fig 2a are shown. For each colored circle, the perimeter represents data point and the interior represents the model. The more similar the perimeter and interior colors, the better the fit of the model to the data.
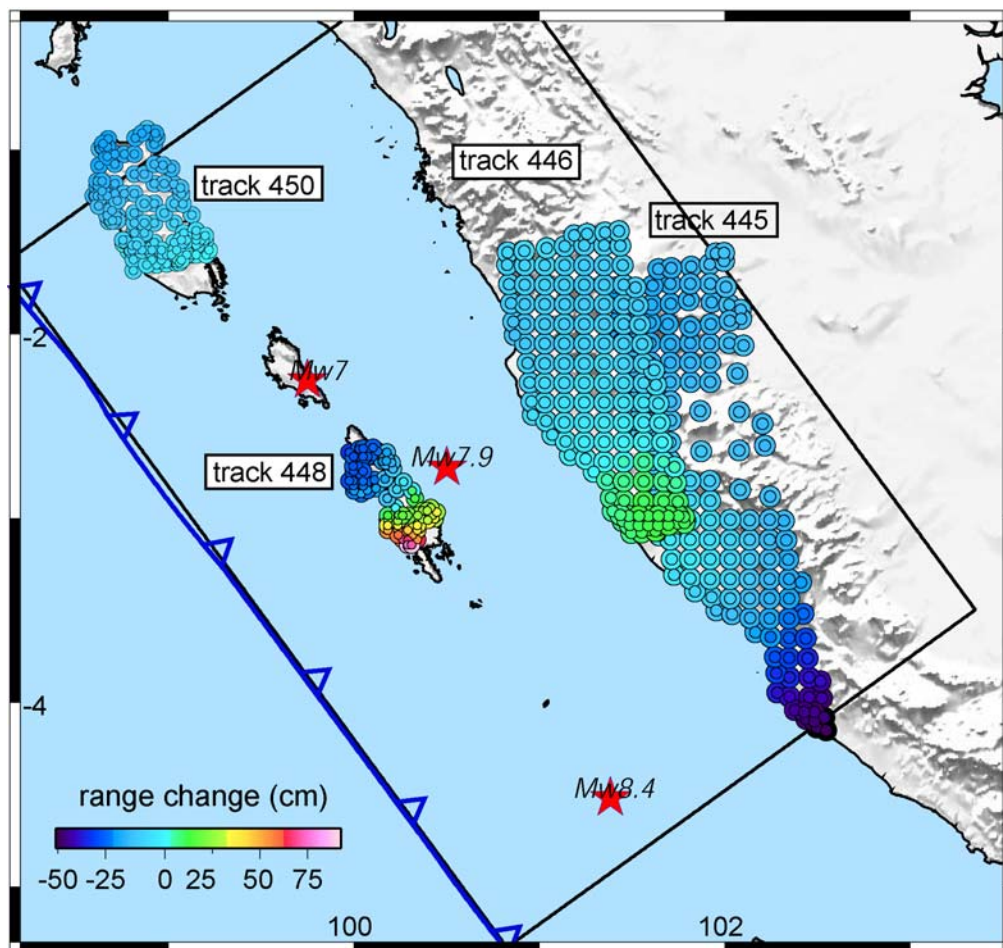
Figure S2 | Source model of the cumulative slip using coseismic measurements | a Cumulative-slip model derived from the inversion of the cGPS data only. Observed (black) and modeled (green for horizontal and gray for vertical) displacement vectors at the SuGAr GPS stations. **b** Cumulative slip obtained from addition of coseismic models of M_w 8.4 and M_w 7.9 earthquakes along with an M_w 7 aftershock located at the northwestern tip of Sipora Island. All three earthquake epicenters are shown with red stars.
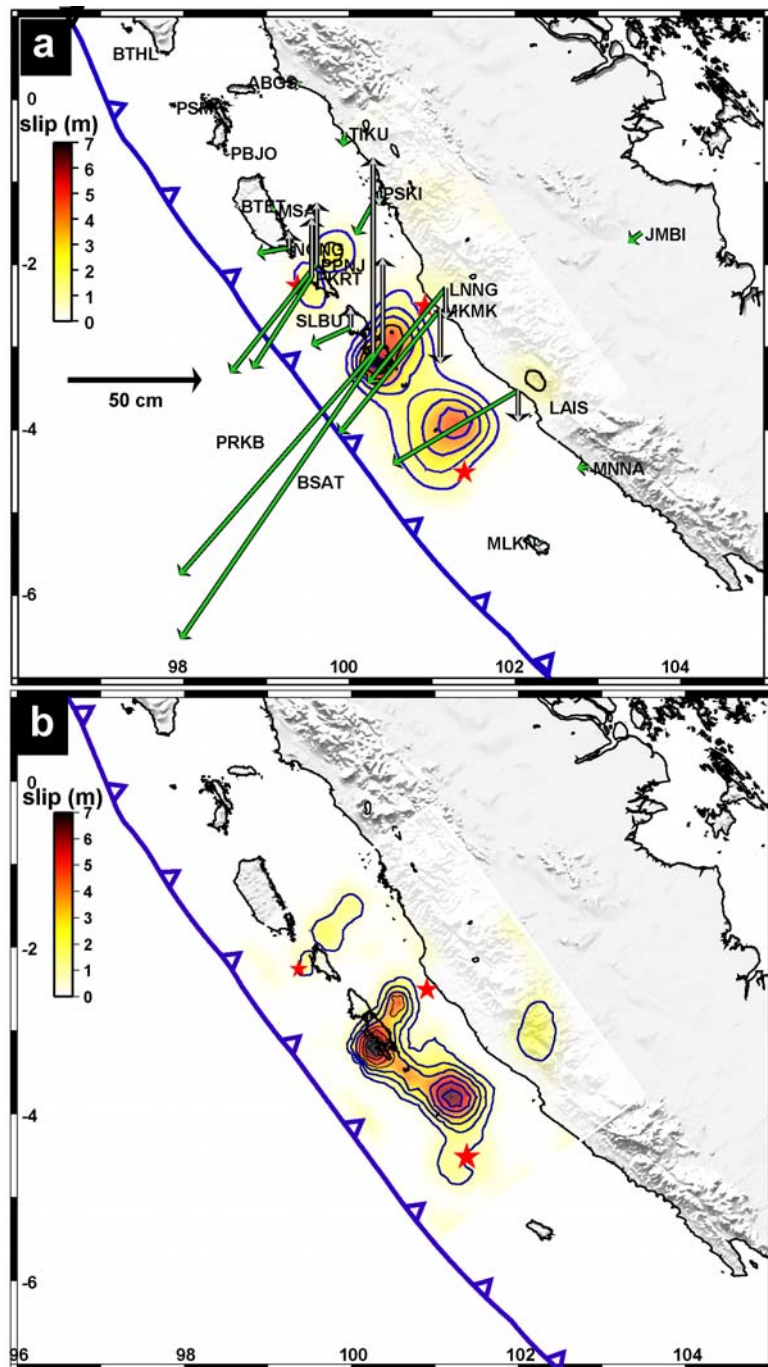
Figure S3 | Cumulative slip due to the whole earthquake sequence obtained from the inversion of the GPS and InSAR data in assuming a down-dip increase of the megathrust dip angle. Dip angle is 10° in the shallower depths (red box) and is 20° further away from the trench (orange box).
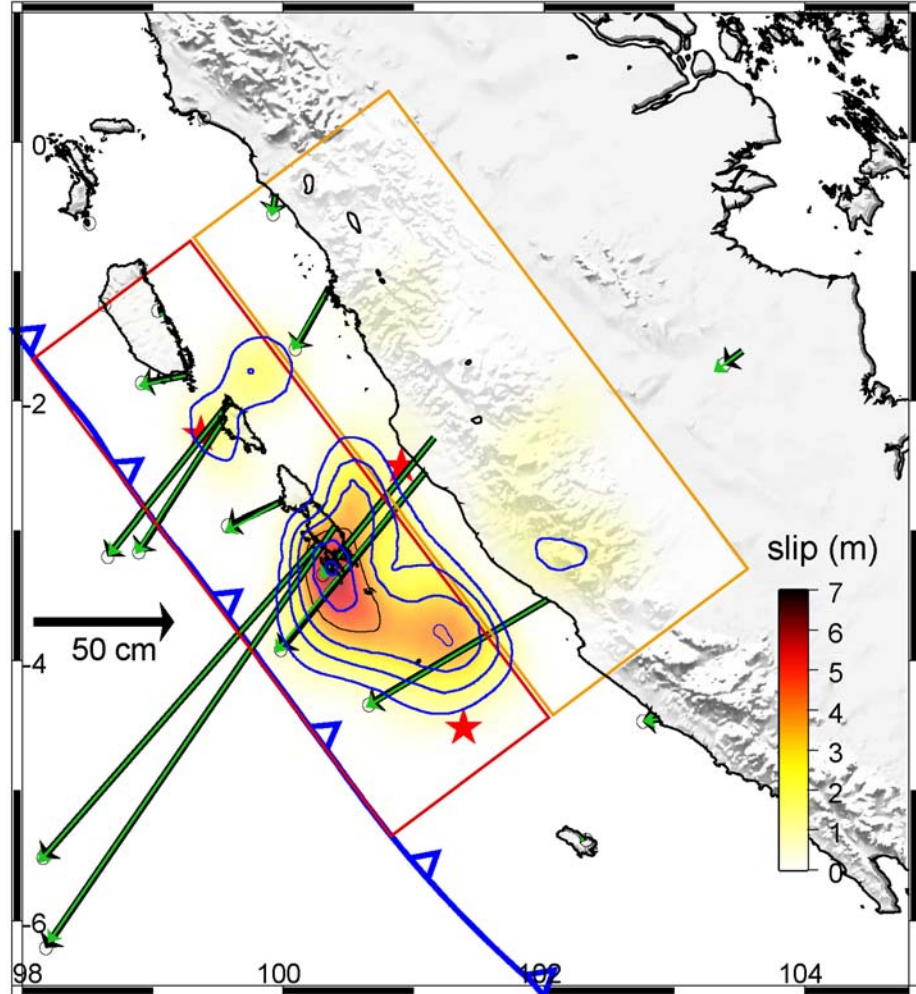
Figure S4 | Checkerboard resolution tests. a Input slip distribution corresponding to 80 km × 80 km slip patches (left) and model (right) derived from the inversion of the synthetic GPS and InSAR data. **b** Input slip distribution corresponding to 48 km × 48 km slip patches (left) and model (right) derived from the inversion of the synthetic GPS and InSAR data.
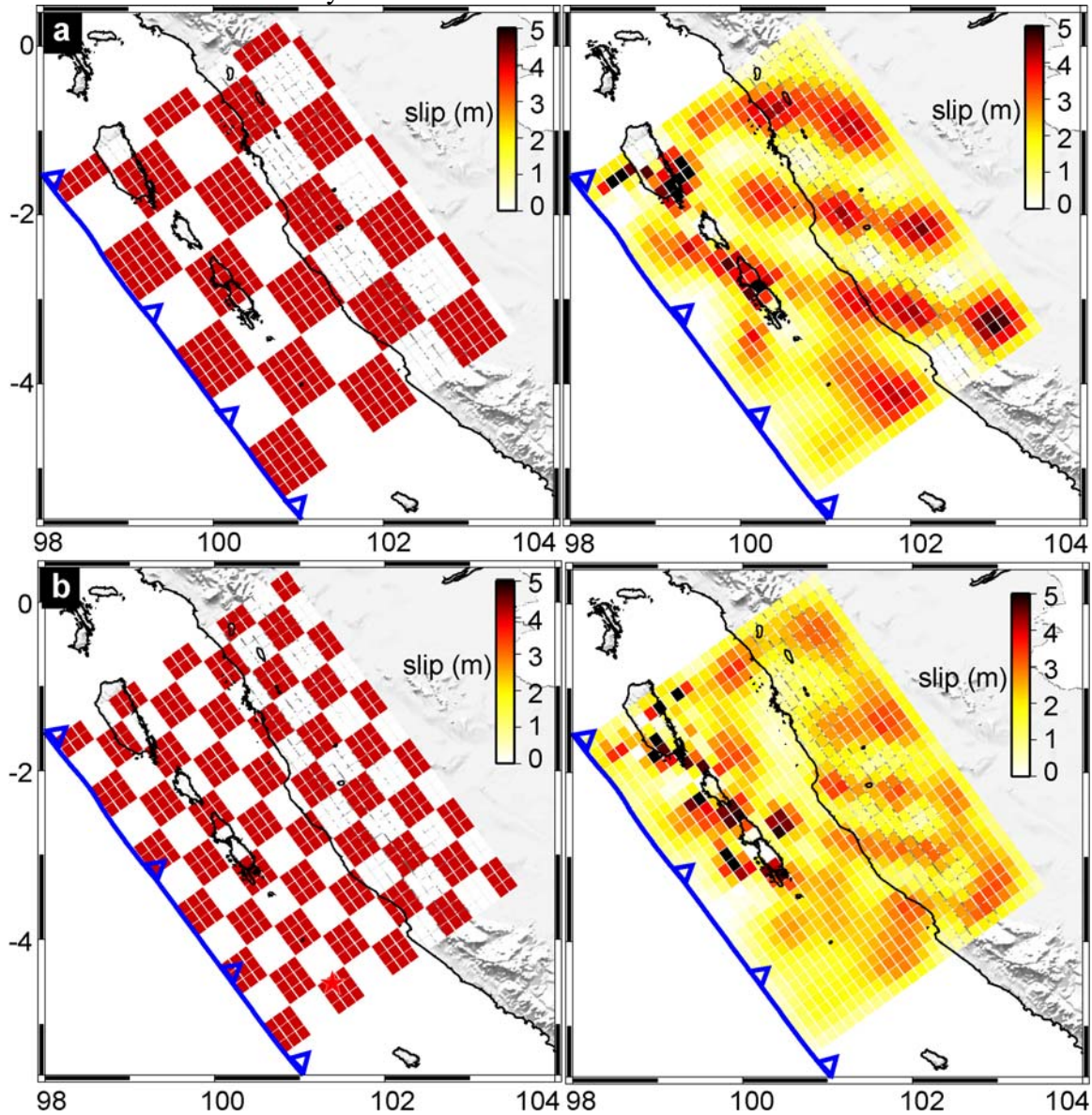
Figure S5 | Source models of M$_w$ 8.4 and 7.9 earthquakes derived from the inversion of the teleseismic records only. Slip distribution of the M$_w$ 8.4 earthquake **(a)**, and M$_w$ 7.9 earthquake **(b)**.
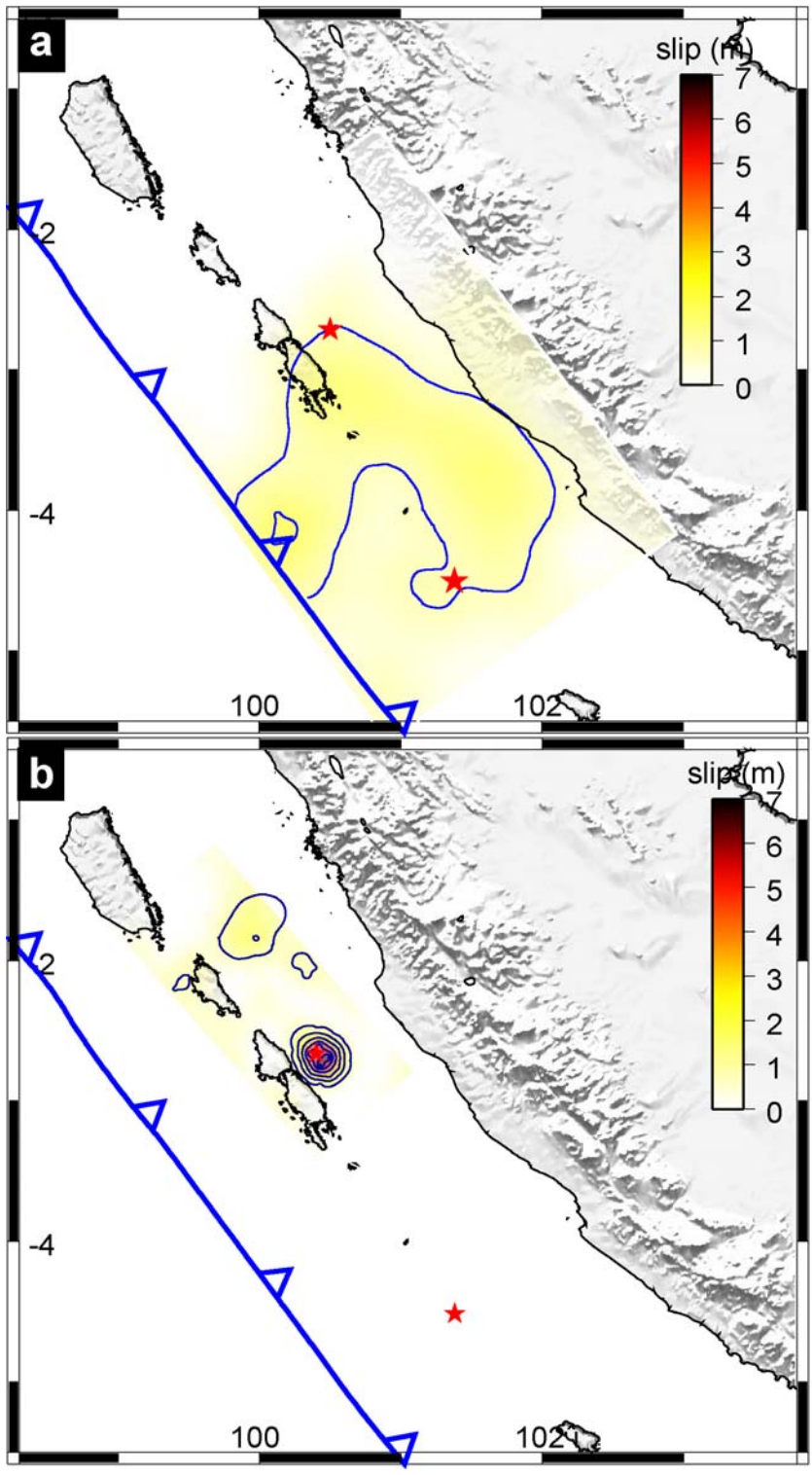
Figure S6 | Comparison of observed and predicted InSAR and teleseismic data, in the joint inversion for the M$_w$8.4 mainshock. a Observed and modeled LOS displacements to the InSAR data. Only the southernmost track (track 445), where the effect of the 7.9 earthquake can be assumed negligible, was used to constrain this event. For each colored circle, the perimeter represents data and the interior represents the model. The more similar the perimeter and interior colors, the better the fit of the model to the data. **b** Observed (black) and synthetic (red) teleseismic *P* and *SH* waveforms. Station name, azimuth, and distance are indicated on the left of each trace. The maximum displacement is shown at the top right of each trace in microns.
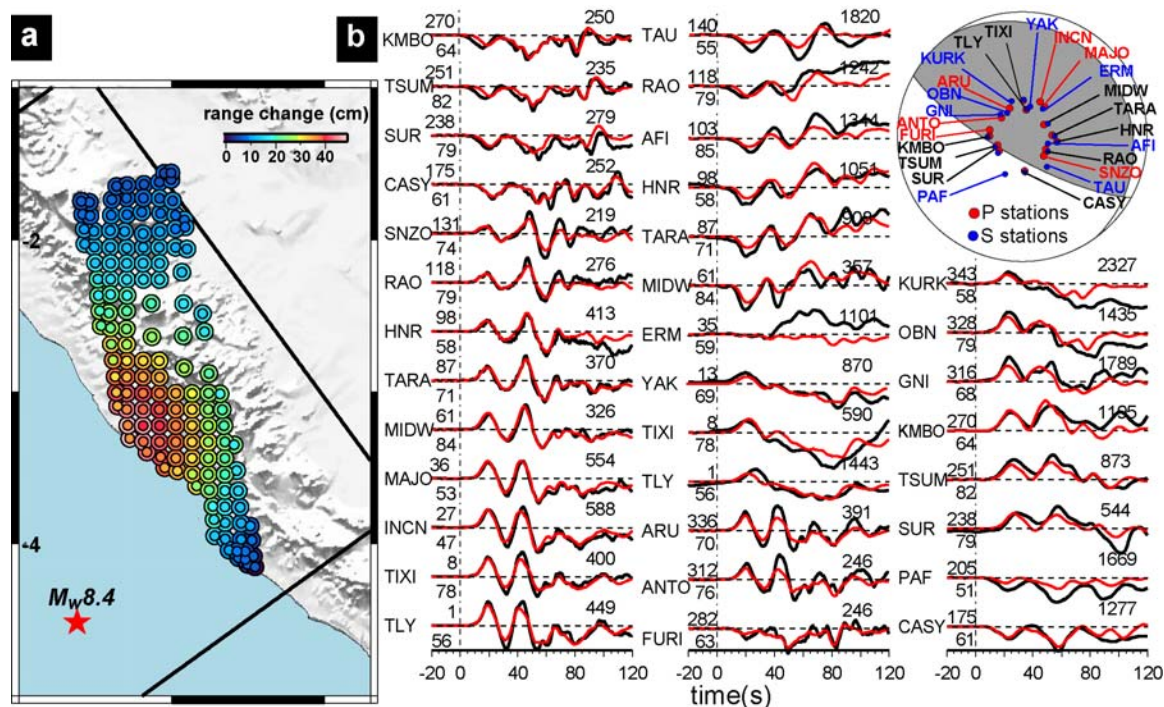
Figure S7 | M$_w$7.9 joint inversion model fits to the teleseismic data. Observed (black) and synthetic (red) teleseismic *P* and *SH* waveforms. Station name, azimuth, and distance are indicated on the left of each trace. The maximum displacement is shown at the top right of each trace in microns.
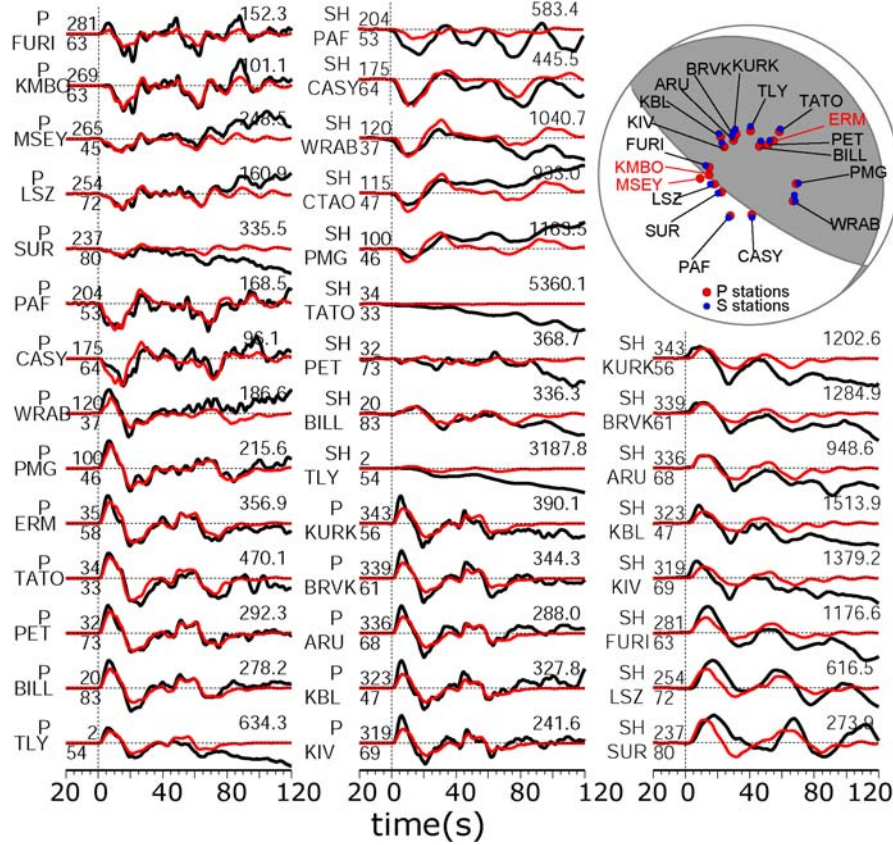
Figure S8 | Distribution of slip, isochrons and rise time for the M$_w$8.4 (a) and 7.9 (b) earthquakes.
Top plots show the final slip distribution on the fault plane and position of the rupture front every 20 s.
Arrows at each sub-fault represent the slip direction of the hanging wall relative to the footwall. Their
size is proportional to slip. Rise time is defined as the duration of slip on each sub-fault.
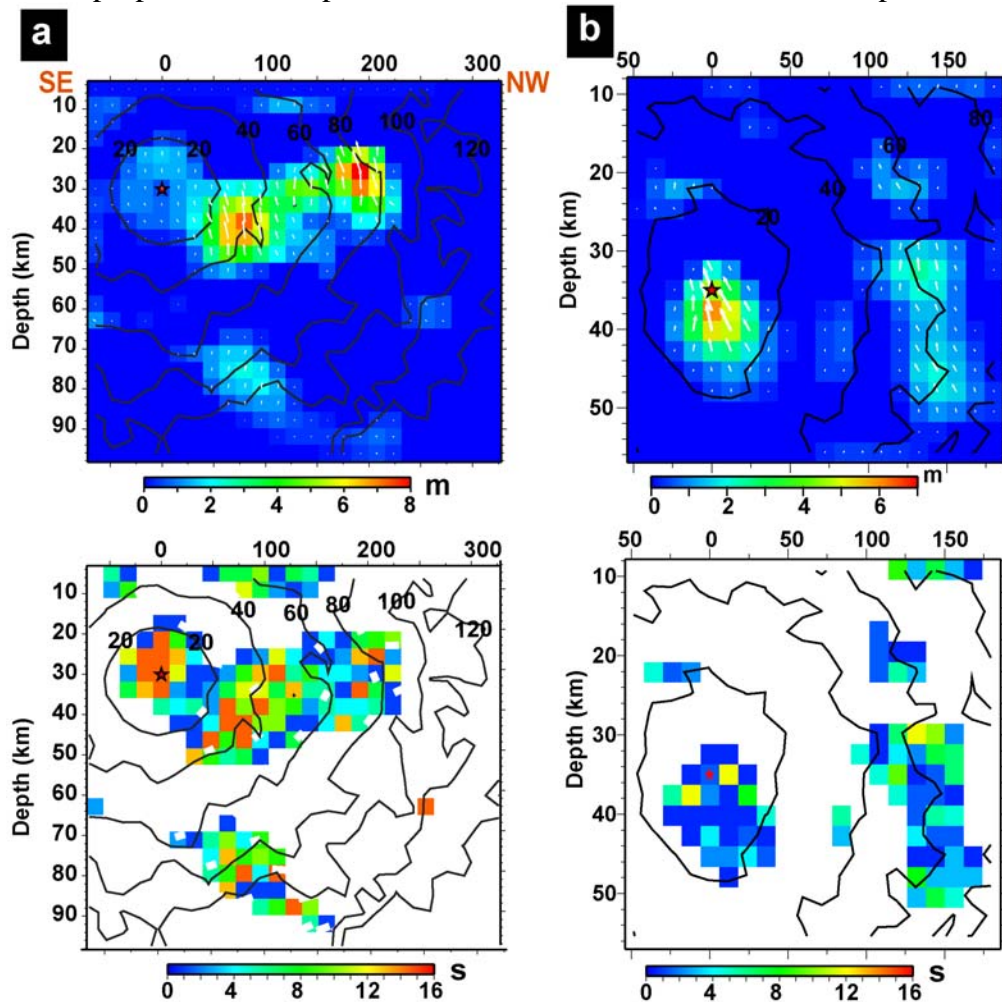
Figure S9 | Influence of a deep patch on surface displacements at LAIS. Measured horizontal (black) and vertical (blue) displacements at LAIS station are compared to model predictions when the deep slip patch is either included (model 1) or removed (model 2). "Model 1" is the model with slip down to 90 km as shown in Fig. 2b and Fig. S4a. "Model 2" has no slip deeper than 60 km, hence slip is confined to the area southwest (trenchward) of LAIS. Model 2 underestimates horizontal displacement but overestimates subsidence at LAIS. Improving the fits to the horizontal displacements worsens the fits to the vertical data, since additional slip up-dip of the LAIS station creates even greater subsidence.
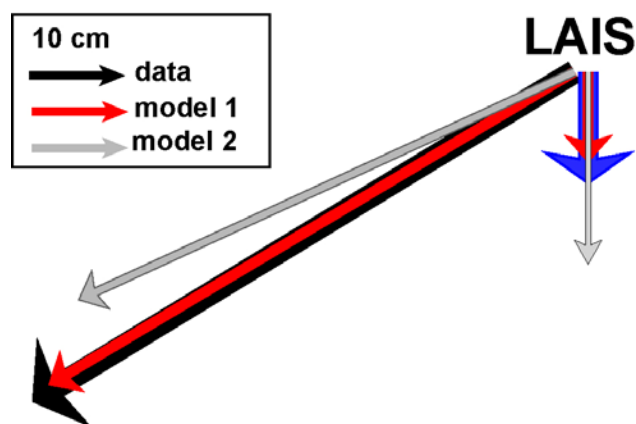
Figure S10 | Moment rate for the M$_w$ 8.4 and M$_w$ 7.9 events. The black and green curves show the source time functions of the mainshock and aftershock, respectively. The red curve is the source time function of the mainshock where slip patches deeper than 65 km are removed from the model. The similarity of the red and black curves shows that the deeper portion's contribution to the moment rate is very smooth, and details of the moment release are determined by the shallower slip patches.
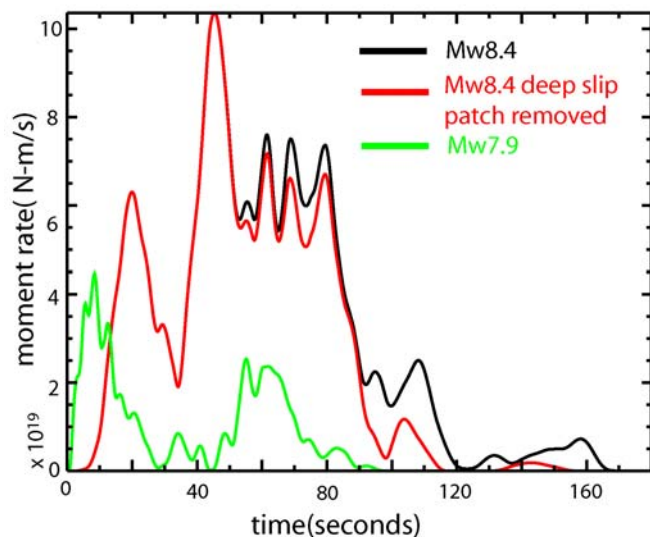
Table S1 : Cumulative co-seismic displacements due to the M_w 8.4 and 7.9 earthquakes and uncertainties derived from the GPS time series.

name	lon	lat	z	n	E	σ_z	σ_n	σ_e
ABGS	99.38749	0.22082	-0.6513	-1.6205	0.3712	0.51	0.13	0.19
BAKO	106.85000	-6.49000	-0.9400	0.5197	-0.0900	0.45	0.10	0.14
BITI	97.81137	1.07862	-0.9501	0.3598	-0.0797	0.77	0.16	0.21
BSAT	100.28456	-3.07669	72.9650	-113.0958	-98.7871	0.70	0.15	0.22
BSIM	96.32616	2.40925	-0.1753	0.5168	0.1224	0.68	0.16	0.21
BTET	98.64394	-1.28155	-1.3305	1.1137	-0.5895	0.52	0.13	0.19
BTHL	97.71070	0.56920	-0.4527	0.3365	0.0305	0.54	0.14	0.19
JMBI	103.52033	-1.61564	-0.2283	-4.7593	-6.4266	0.64	0.15	0.20
LAIS	102.03394	-3.52923	-11.7705	-37.5981	-64.0160	0.65	0.15	0.20
LEWK	95.80406	2.92359	-0.8573	0.4220	0.0490	0.52	0.14	0.18
LNNG	101.15646	-2.28531	-11.6927	-48.6283	-39.6428	0.52	0.14	0.19
MKMK	101.09140	-2.54264	-20.3530	-63.5146	-51.5661	0.53	0.14	0.19
MLKN	102.27649	-5.35255	-2.0100	-1.3571	2.2129	0.77	0.15	0.21
MNNA	102.89026	-4.45033	-1.9415	-0.8341	-6.0903	0.63	0.15	0.21
MSAI	99.08948	-1.32642	-1.2953	1.0095	-2.3344	0.69	0.16	0.22
NGNG	99.26829	-1.79959	5.7611	-2.9307	-16.4728	0.71	0.15	0.21
NTUS	103.67990	1.34580	-0.9974	-1.9993	-1.2960	0.44	0.12	0.16
PBJO	98.51571	-0.63651	-1.6725	0.3336	-0.0090	0.80	0.15	0.22
PBLI	97.40528	2.30852	0.0091	0.2268	0.1089	0.52	0.14	0.19
PKRT	99.54279	-2.15138	22.0024	-46.8171	-30.1824	0.84	0.17	0.24
PPNJ	99.60369	-1.99400	22.8536	-55.6964	-44.0273	0.60	0.14	0.20
PRKB	100.39961	-2.96660	32.1723	-150.3399	-103.1441	0.61	0.14	0.20
PSKI	100.35340	-1.12468	-4.9449	-21.9466	-12.0874	0.83	0.18	0.26
PSMK	97.86091	-0.08931	-0.6677	0.0930	-0.0754	0.60	0.14	0.19
SAMP	98.71471	3.62161	-0.7795	0.0009	-0.0001	0.61	0.15	0.20
SLBU	100.00967	-2.76634	7.4130	-9.0250	-20.2186	0.67	0.15	0.21
TIKU	99.94418	-0.39913	-0.7476	-7.3503	-1.0042	0.62	0.15	0.21

Table S2 : Co-seismic displacements due to the M_w 8.4 earthquake and uncertainties derived from the GPS time series.

name	lon	lat	z	n	e	σ_z	σ_n	σ_e
ABGS	99.38749	0.22082	-2.2354	-0.7124	1.8591	0.58	0.15	0.21
BAKO	106.85000	-6.49000	-0.0024	-0.6192	1.5462	0.52	0.12	0.15
BITI	97.81137	1.07862	-2.4067	-0.5641	1.6590	0.92	0.18	0.24
BSAT	100.28456	-3.07669	61.1763	-87.2345	-81.1502	0.83	0.18	0.25
BSIM	96.32616	2.40925	-1.6402	-0.3919	1.8470	0.80	0.18	0.23
BTET	98.64394	-1.28155	-1.3127	-0.6443	1.7655	0.61	0.15	0.21
BTHL	97.71070	0.56920	-2.7656	-0.5087	1.8299	0.60	0.15	0.21
JMBI	103.52033	-1.61564	-0.8869	-4.9008	-2.7951	0.70	0.16	0.22
LAIS	102.03394	-3.52923	-12.3301	-36.4582	-59.9395	0.74	0.16	0.23
LEWK	95.80406	2.92359	-1.9170	-0.5406	1.7558	0.58	0.15	0.20
LNNG	101.15646	-2.28531	-4.2030	-33.6649	-14.8307	0.57	0.15	0.21
MKMK	101.09140	-2.54264	-11.8656	-52.4408	-28.9090	0.64	0.15	0.21
MLKN	102.27649	-5.35255	-2.9891	-2.1924	3.4817	0.95	0.17	0.24
MNNA	102.89026	-4.45033	-2.7864	-1.4762	-4.0612	0.74	0.17	0.23
MSAI	99.08948	-1.32642	-0.5374	-0.9746	2.1352	0.71	0.16	0.22
NGNG	99.26829	-1.79959	-3.4996	-1.0757	2.1772	0.83	0.17	0.23
NTUS	103.67990	1.34580	0.2959	-1.4613	1.4697	0.48	0.13	0.17
PBJO	98.51571	-0.63651	-0.5590	-0.1682	1.9071	0.95	0.18	0.25
PBLI	97.40528	2.30852	-1.4433	-0.2905	1.8579	0.59	0.15	0.21
PKRT	99.54279	-2.15138	-3.7057	-1.2220	1.7142	1.03	0.20	0.27
PPNJ	99.60369	-1.99400	-2.6877	-1.7239	2.0305	0.67	0.16	0.22
PRKB	100.39961	-2.96660	-11.2013	-95.5292	-71.5242	0.71	0.16	0.22
PSKI	100.35340	-1.12468	-1.2549	-5.0834	1.5760	0.88	0.19	0.27
PSMK	97.86091	-0.08931	-1.8826	-0.3429	1.7369	0.69	0.16	0.22
SAMP	98.71471	3.62161	-0.3348	-0.0010	-0.0014	0.74	0.19	0.25
SLBU	100.00967	-2.76634	-1.1477	-3.1006	-3.9084	0.74	0.16	0.23
TIKU	99.94418	-0.39913	-3.8457	-3.2957	1.9442	0.73	0.17	0.24

Table S3 : Co-seismic displacements due to the M_w 7.9 earthquake and uncertainties derived from the GPS time series.

name	lon	lat	z	n	e	σ_z	σ_n	σ_e
ABGS	99.38749	0.22082	-0.5913	-0.2557	-0.8977	2.11	0.40	0.52
BAKO	106.85000	-6.49000	-0.8924	0.6740	-1.0531	1.12	0.22	0.30
BITI	97.81137	1.07862	1.6272	0.7937	-1.4707	2.46	0.39	0.51
BSAT	100.28456	-3.07669	12.9069	-22.2555	-14.0978	2.23	0.41	0.59
BSIM	96.32616	2.40925	0.6418	0.8179	-1.6020	2.11	0.40	0.51
BTET	98.64394	-1.28155	-0.5056	1.5041	-1.7813	1.79	0.35	0.47
BTHL	97.71070	0.56920	1.6883	2.7985	-1.8515	2.45	0.42	0.56
JMBI	103.52033	-1.61564	-0.0795	0.2519	-2.4870	1.85	0.36	0.50
LAIS	102.03394	-3.52923	-0.7157	0.0463	-2.0763	1.93	0.38	0.51
LEWK	95.80406	2.92359	0.5571	0.6526	-1.6152	1.63	0.34	0.45
LNNG	101.15646	-2.28531	-8.5442	-11.9588	-22.4762	1.85	0.37	0.50
MKMK	101.09140	-2.54264	-7.1612	-8.3046	-19.7675	1.57	0.33	0.46
MLKN	102.27649	-5.35255	2.0745	0.8419	-1.3896	2.57	0.39	0.53
MNNA	102.89026	-4.45033	-0.1754	0.5802	-1.1920	1.70	0.35	0.49
MSAI	99.08948	-1.32642	-0.0545	2.0363	-3.3772	1.95	0.37	0.49
NGNG	99.26829	-1.79959	7.7647	-1.3524	-17.2423	2.28	0.39	0.52
NTUS	103.67990	1.34580	-1.0845	-0.5629	-2.2186	0.95	0.24	0.30
PBJO	98.51571	-0.63651	-2.1201	0.3516	-2.0179	3.27	0.47	0.61
PBLI	97.40528	2.30852	5.7982	-0.3303	-1.5957	1.94	0.40	0.51
PKRT	99.54279	-2.15138	20.2666	-27.8907	-19.8954	2.17	0.42	0.57
PPNJ	99.60369	-1.99400	29.6427	-37.8411	-36.6640	1.69	0.34	0.47
PRKB	100.39961	-2.96660	42.3380	-51.9952	-27.6695	2.14	0.40	0.55
PSKI	100.35340	-1.12468	-5.7231	-15.5925	-12.6022	2.49	0.43	0.61
PSMK	97.86091	-0.08931	3.3596	1.4010	-0.9709	2.34	0.41	0.53
SAMP	98.71471	3.62161	0.1076	0.0012	0.0007	1.34	0.48	0.61
SLBU	100.00967	-2.76634	9.2680	-5.2968	-14.9048	1.97	0.38	0.53
TIKU	99.94418	-0.39913	1.4097	-4.1663	-1.7832	2.93	0.48	0.69

Table S4 Uplift measured from emerged coral heads.

Site	Latitude	Longitude	Measurement Date	Uplift(cm)	Uncertainty (2 σ, cm)
MEG07-A	-4.00671	101.03388	10/06/07	135	14
MEG07-B	-4.01665	101.03865	10/06/07	125	6
STP07-A	-3.45356	100.68337	10/06/07	20	12
SDG07-A	-3.48633	100.63690	10/07/07	93	23
TBO07-A	-3.34554	100.46660	10/07/07	91	14
LMS07-A	-3.20879	100.33055	10/07/07	99	23
TNP07-A	-3.16373	100.50640	10/08/07	45	12
TNK07-A	-3.18605	100.40586	10/08/07	78	23
LBT07-A	-3.11618	100.22888	10/08/07	83	6
PJS07-A	-3.01587	100.15750	10/09/07	35	12
SPG07-A	-2.88574	100.17689	10/09/07	-3	14
BSG07-A	-2.83829	100.18412	10/09/07	-19	14
TNG07-A	-2.82080	100.28000	10/09/07	-3	18
MBL07-A	-2.51578	100.01300	10/09/07	0	14
TMS07-A	-2.01886	99.61142	10/10/07	≥ 5	12
SGS07-A	-2.04684	99.65144	10/10/07	10	6
RKT07-A	-2.11664	99.70752	10/10/07	20	14
SMY07-A	-2.60447	100.11115	09/30/07	0	18

Table 5: Information about the interferograms computed from ALOS PALSAR images. All images were acquired on ascending tracks.

Region	Track	Frame numbers	Acquisition date 1	Acquisition date 2	Mode [1]	$B_\perp$(m) [2]
Bengkulu	445	7	29-Jan-07	16-Sep-07	FBS2FBD	141
	446	2	18-Aug-07	03-Oct-07	FBD2FBD	268
Pagai	448	1	06-Aug-07	21-Sep-07	FBD2FBD	506
Siberut	450	1	09-Sep-07	25-Oct-07	FBD2FBD	58

[1] FBS: Fine Beam Single Polarization (HH, 28 MHz bandwidth); FBD: Fine Beam Dual polarization (HH and HV, 14 MHz) [20].

[2] $B_\perp$ is the perpendicular baseline, that is, the component of the orbital separation perpendicular to the line of sight.

Table S6: Misfits and normalized uncertainties.

Model	Moment (N-m)	Waveform Misfit	GPS (cm)			Coral (cm)	InSAR (cm)
			σ_e	σ_n	σ_z		
Cumulative (GPS only)	7.3×10^{21}	-	0.9	1.	0.9	-	-
Cumulative (all data)	7.5×10^{21}	-	0.9	1.1	1.0	11.15	1.48
M_w 8.4	5.15×10^{21}	0.14	2.4	2.2	4.1	7.4	3.6
M_w 7.9	1.13×10^{21}	0.25	2.6	2.6	2.3	-	-
M_w 7.0	4.7×10^{19}	-	1.7	2.2	1.5	-	-

Table S7: Weighted Root Mean Square (WRSS) of residuals between the predicted and observed GPS and coral measurements.

Model	GPS			Coral
	E	N	Z	
Cumulative (all data)	18.4	36	6.2	5
M_w8.4	59.2	72	5.4	1.6
M_w7.9	8	7.4	1.5	-